



The imprint of global magma oceans on exoplanet demographics

MARTIN SCHLECKER¹ AND AL.

¹*Department of Astronomy/Steward Observatory, The University of Arizona, 933 North Cherry Avenue, Tucson, AZ 85721, USA*

ABSTRACT

... magma oceans ...

Here, we assess the ability of space and ground-based telescopes to test this hypothesis using Bioverse, a simulation framework that leverages contextual information from the overall planet population. ...

1. INTRODUCTION

...just dropping material and references for now...

papers: (, introduce runaway GH) (Turbet et al. 2019, statistical detection of GH transition), (Luger & Barnes 2015, water loss, O₂ buildup around M dwarfs), (???, Solubility of H in magma oceans) Hamano et al. (2013, 2015); Barth et al. (2021); Downey et al. (2022).

“Points for the intro: Bioverse
Transit survey to measure mass/radius of planets
Does the HZ have an inner edge?
Run-away GH
Magma oceans
Mention missions that are NOT statistical and therefore not considered here: CHEOPS, ARIEL, Roman. Other missions/concepts do not directly measure radii and not considered here: Habitable Worlds Observatory, LIFE.
In contrast, PLATO and Nautilus are
Possibility of follow-up to measure masses ”

For observations of rocky exoplanets, the currently best-probed regime is that of warm, close-in planets. These bodies experience climatic conditions that are similar to the environment of the inner Solar System bodies at early stages of their formation. Studies of the geophysical state and evolution of hot exoplanets can thus contribute to our understanding of the early formation stages of Earth and other habitable worlds.

Venus and Earth, while having accreted from the same mass reservoir and despite their similar bulk properties, evolved into planets with very different environmental conditions on their surfaces. At the formation of the Solar System, both planets underwent a giant impact phase [CITE!] that melted their mantles, leading to a magma ocean stage. Due to these similar early formation phases, it was commonly assumed that the divergence of Venus and Earth – in particular Venus’s water loss – occurred late in their evolution (Elkins-Tanton 2013). Hamano et al. (2013) showed that such a late desiccation process is not needed to explain the stark differences: for a planet rich in volatiles and receiving high enough radiation levels from its host star, a steam atmosphere limits the outgoing radiation from the (molten) planetary surface. This runaway greenhouse state prevents the planet’s

rapid cooling and can extend the magma ocean stage to hundreds of Myr, enough to remove the entire water reservoir from a rocky planet by hydrodynamic escape.

important for motivating the existence of the pattern: "the solidification timescale can become comparable to the main-sequence lifetime of the star (Hamano et al. 2013, 2015)" (Lichtenberg et al. 2022)

Consequently, it is aptly considered to be the inner boundary of the habitable zone (Kasting et al. 1993; Kopparapu et al. 2013).

(Under the right conditions, different orbital distances alone can thus decide about a planet's water content and ultimately its habitability.) If received flux makes the difference between our own habitable planet and dry, dead Venus, there is good reason to believe that such patterns exist in exoplanet systems as well.

...long-term goal/overarching objective: derive the geophysical history of rocky extrasolar planets. More concrete: Constrain the limits of runaway greenhouse transitions, and thus the inner edges of the habitable zone. Also: How close is Earth from this runaway greenhouse irradiation limit? ...

introduce magma oceans and their influence on planetary radii (Dorn & Lichtenberg 2021).

...current/future observations of planets that are currently in the runaway greenhouse phase may constrain properties of their planetary mantles... make connection between interior and atmospheres. ... Planetary radius changes due to the combined effect of steam atmospheres and water dissolved in the molten mantle of planets within the runaway greenhouse threshold is expected to cause a discontinuity in the radius distribution of small (DEFINITION) exoplanets.

2. METHODS

Start methods description with brief statement of goal and overview of the steps. The first sentence is similar, but would be good to separate goal from method here.

We determined – for different survey configurations – the confidence level with which the runaway greenhouse threshold can be detected in simulated exoplanet observations. For this purpose we expanded the Bioverse framework (Bixel & Apai 2020, 2021)¹ to generate synthetic stellar and planetary samples into which we injected the runaway greenhouse signal, simulated observations of this sample, and computed Bayesian evidences in favor of the runaway greenhouse hypothesis (see diagram in Fig. 1).

Bioverse will need a short introduction before the modifications are mentioned. Probably should get a paragraph in the intro

2.1. *Synthetic star and planet sample*

In the following, we review the source of the stellar sample, the modeled luminosity evolution, the generation of a synthetic planet sample, as well as the orbital parameters of the planets.

2.1.1. *Stellar sample from Gaia DR3*

¹ Bioverse is actively maintained and documented open source software written in Python. Its latest version and documentation can be found at <https://github.com/danielapai/bioverse>.

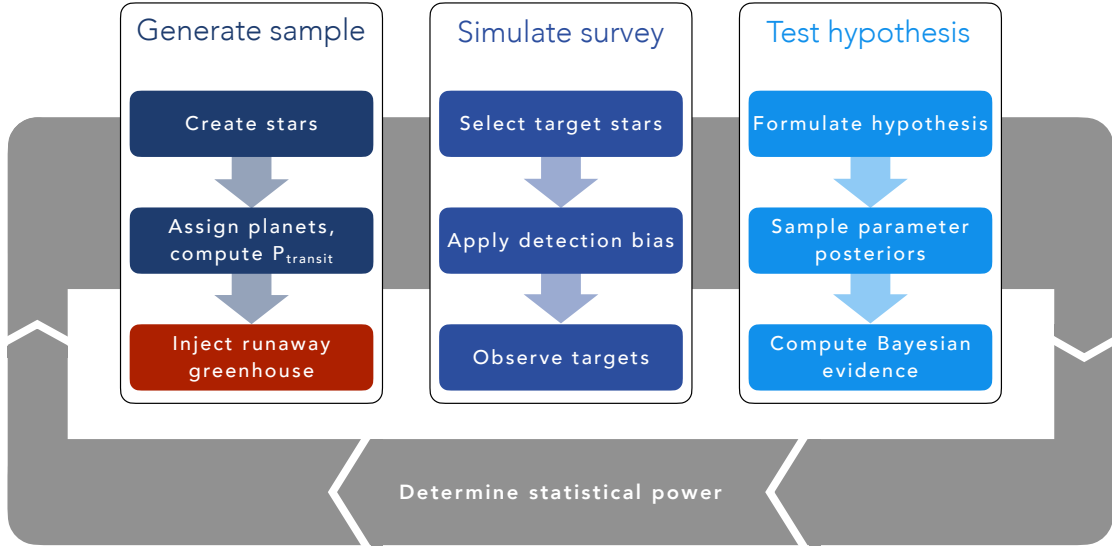


Figure 1. Workflow of our hypothesis testing with Bioverse. In the first block, we generate a sample of stars and populate them with planets based on *Kepler* demographics. A fraction of them are then assigned a runaway greenhouse climate based on the model described in Sect. 2.1.6. The second block simulates an exoplanet survey, whereby selection effects and detection biases are introduced. Finally, the third block deals with testing the runaway greenhouse hypothesis based on data from the survey simulation. By iterating through these steps, we compute the statistical power of testing the hypothesis given the assumed survey design.

KEVIN: describe stellar population

...

2.1.2. Stellar luminosity evolution

Planetary systems are hosted by stars of a wide range of ages, and stellar luminosities evolve with time. Since the emergence of a runaway greenhouse phase on a planet is highly dependent on the level of radiation it receives, and thus on the luminosity of the host star, we assigned age-dependent luminosities to our synthetic stars.

While stellar ages are notoriously poorly constrained (e.g., Adams et al. 2005), the age distribution of planet host stars in the Solar neighborhood was shown to be broadly consistent with uniform (Reid et al. 2007; Gaidos et al. 2023). For our synthetic stars, we thus drew random ages from a uniform distribution from 0 Gyr to 10 Gyr. We then assigned each star a luminosity from the mass-dependent evolutionary models in Baraffe et al. (1998). Figure 2 shows the corresponding luminosity evolution as a function of stellar mass and age.

2.1.3. Synthetic planet sample

Next, we assigned to the stellar sample planetary systems with frequencies, orbital parameters, and bulk properties derived from the *Kepler* mission. We adopted the planetary occurrence rates in orbital period and radius recently derived in Bergsten

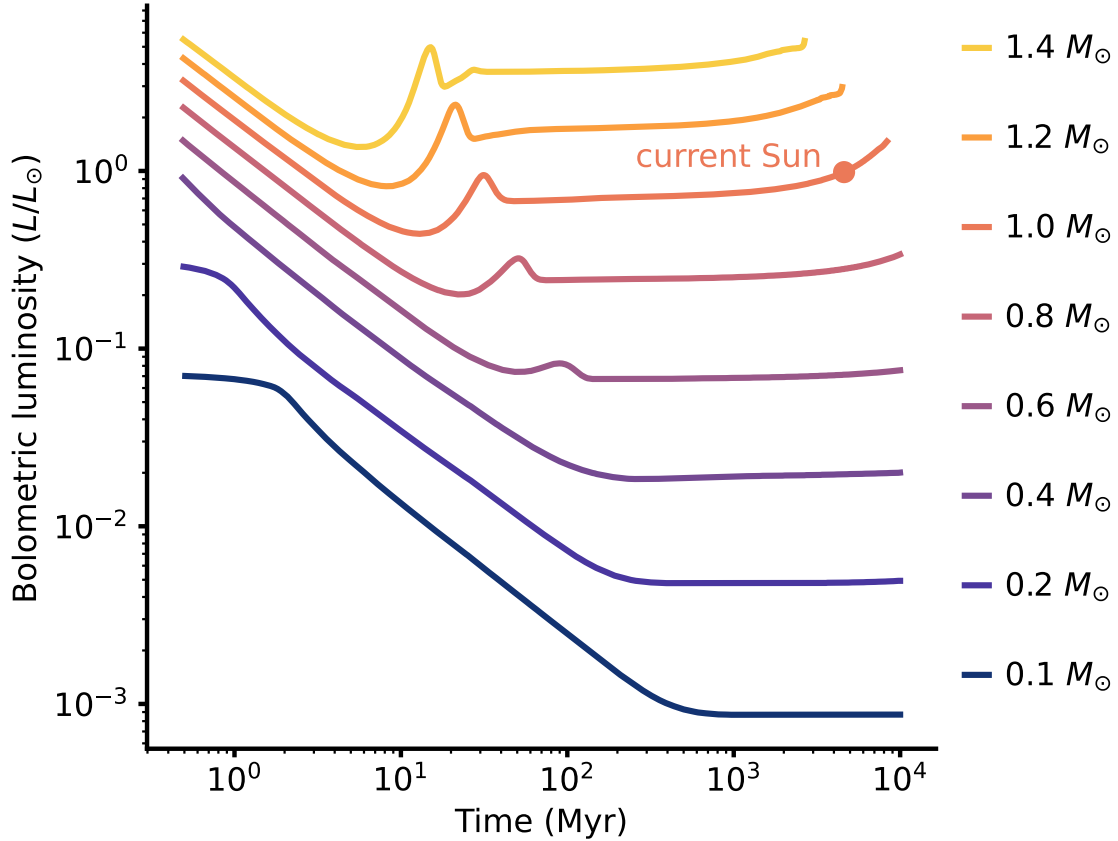


Figure 2. Bolometric luminosity tracks of stars with different masses, computed from stellar evolution models in Baraffe et al. (1998). Low-mass stars, which make up the majority of stars in the solar neighborhood, undergo an extended early phase of several magnitudes higher luminosity before entering a lifetime of relative faintness.



et al. (2022). Following Youdin (2011), their inferred occurrence rate density can be expressed in the form

$$\frac{d^2n}{dR dP} = F_0 C_n g(R, P), \quad (1)$$

where F_0 ...

GALEN: Briefly describe underlying planet occurrence rates of synthetic population, its Mstar dependency, any caveats or assumptions.

2.1.4. Orbit parameters and planet masses

Eccentric orbits alter the probability of a planet to transit (e.g., Barnes 2007). The distribution of eccentricities e of exoplanets has been found to resemble a Beta function (Kipping 2013), which we chose to draw synthetic eccentricities from. Following Kipping (2013), we used a Beta distribution with parameters $a = 0.867$ and $b = 3.03$, and truncated the distribution at $e = 0.8$. Assuming isotropic alignments of orbits, we assigned each planet an inclination drawn from a distribution uniform in $\cos(i)$.

To assign masses to our planets, we use the semi-empirical mass-radius relationship assuming a pure MgSiO_3 composition from [Zeng et al. \(2016\)](#) (see green line in Fig. 3). This represents the baseline bulk density before any climate-related effects are applied.

2.1.5. Transit probability

We model the occurrence of transits by assuming isotropic orientations of planetary orbits, calculating the impact parameters $b = \cos(i)/R_\star$ and considering only observable planets with $|b| < 1$. For these cases we calculate the transit depth

$$\delta = \left(\frac{R_P}{R_\star} \right)^2, \quad (2)$$

which is relevant for the detection probability of the respective planet (see Sect. 2.2.1). Excluding all non-transiting planets diminishes the sample to 1.5 % of its original size.

2.1.6. Planet radius changes due to runaway greenhouse climates

The climate state of a planet has a direct influence on its size as measured by transit photometry ([Turbet et al. 2019](#)). Here, we use predictions on transit atmospheric thickness from geophysical models to derive the transit radii of planets with temperate climates and those with instellation-induced runaway greenhouse climates, respectively. ...

ARNAUD: revise definition of S following our discussion on 2022-12-22. Introduce net instellation and clarify what is meant by it.

The power from the host star per unit area at the position of a planet or net instellation S in units of Earth's insolation is given by

$$\frac{S}{S_\oplus} = \left(\frac{L_\star}{L_\odot} \right) \left(\frac{au}{a} \right)^2. \quad (3)$$

Here, we assume global redistribution of incoming flux and a fixed albedo of 0.3, comparable to Earth's ([Haar & Suomi 1971](#)). The absolute value of S_\oplus , by which all synthetic planets are scaled, is then 238 W m^{-2} . We do not take into account additional heating sources such as tidal effects (e.g. [Barnes et al. 2013](#)).

Central to our procedure is to explore the detectability of population-level trends with future exoplanet surveys, and here the trend in question is the proposed radius discontinuity. To enable a quantitative assessment of this detectability, we injected the signal into the simulated planet sample before observing it with simulated surveys. While we search for the runaway greenhouse pattern in demographic quantities such as average planet radii, the injected changes happen on the planetary level: We changed each planet's radius based on its individual set of properties and the associated predictions from steam atmosphere and water incorporation models. Relevant properties are a planet's mass M , its net instellation S , and its bulk water inventory expressed as a water mass fraction $x_{\text{H}_2\text{O}}$. We consider the following cases (see Fig. 3):

Non-runaway planets retain the radius assigned based on exoplanet occurrence rates (see Sect. 2.1.3). This case serves as our null hypothesis.

For all planets receiving a dayside-averaged instellation exceeding a threshold of $S_{\text{thresh}} = 280 \text{ W m}^{-2}$, we assume an inflated radius due to a steam atmosphere. While the actual instellation threshold for a runaway climate depends on planetary albedo, surface gravity, and clouds (Pierrehumbert 2022), this value was found to be a typical limit for the flux a planet can emit in a runaway greenhouse situation (Abe & Matsui 1988; Kasting 1988; Nakajima et al. 1992; Goldblatt et al. 2013; Leconte et al. 2013; Boukrouche et al. 2021). To quantify the radius change, we applied the mass-radius relationships derived by Turbet et al. (2020) using a 1D inverse radiative-convective model (Turbet et al. 2019). Their calculations rely on the same mass-radius relations for rocky interiors that we apply for our non-runaway planets (Zeng et al. 2016). For each planet above the instellation threshold, we assigned the predicted radius for the given water mass fraction and planet mass. This scenario does not take into account the expected additional radius change due to interiors that are molten due to greenhouse forcing (Bower et al. 2019). It further assumes a *dry melt* without dissolved volatiles.

Wet melt planets follow the rules above, but we take into account a radius decrease from water partitioning in the melt: In the situation of a magma ocean below a steam atmosphere, part of the water will partition into the melt. This removes it from the steam atmosphere, which in turn decreases the radius inflation. The effect is generally small compared to the radius inflation from a steam atmosphere but resulting radius changes typically reach measurable values (Dorn & Lichtenberg 2021). The magnitude of this effect is again dependent on the planet mass and on the water mass fraction. We follow Dorn & Lichtenberg (2021) and use their computed radius deviations between a wet magma ocean and a solid mantle for a tropopause pressure $P_{\text{iso}} = 0.1 \text{ bar}$. We then add the (in almost all cases negative) radius deviations to the planet radii computed for the dry melt case.

Figure 3 shows the different mass-radius relations of the three cases for a fiducial water mass fraction of $x_{\text{H}_2\text{O}} = 0.005$. Steam atmospheres cause a significant radius increase, which is slightly reduced when water incorporation in the melt is considered. In the following, we only distinguish between the non-runaway greenhouse and wet melt scenarios.

As illustrated in Fig. 3 (bottom panel), different processes can lead to the classification of a planet into either of these categories. For instance, both a Hydrogen/Helium-dominated “sub-Neptune” and a terrestrial planet currently hosting a steam atmosphere will appear as a planet in our runaway greenhouse category, diluting the expected demographic signature. Further, a planet in a runaway greenhouse state will eventually lose its steam atmosphere and move to the non-runaway greenhouse category on a timescale of 10^8 yr for a planet with one Earth ocean of water (Watson et al. 1981). To account for these effects, we introduce a dilution parameter f_{rgh} , which represents the fraction of planets above the threshold instellation that are currently inflated due to a runaway greenhouse climate. Our simulation setup is such

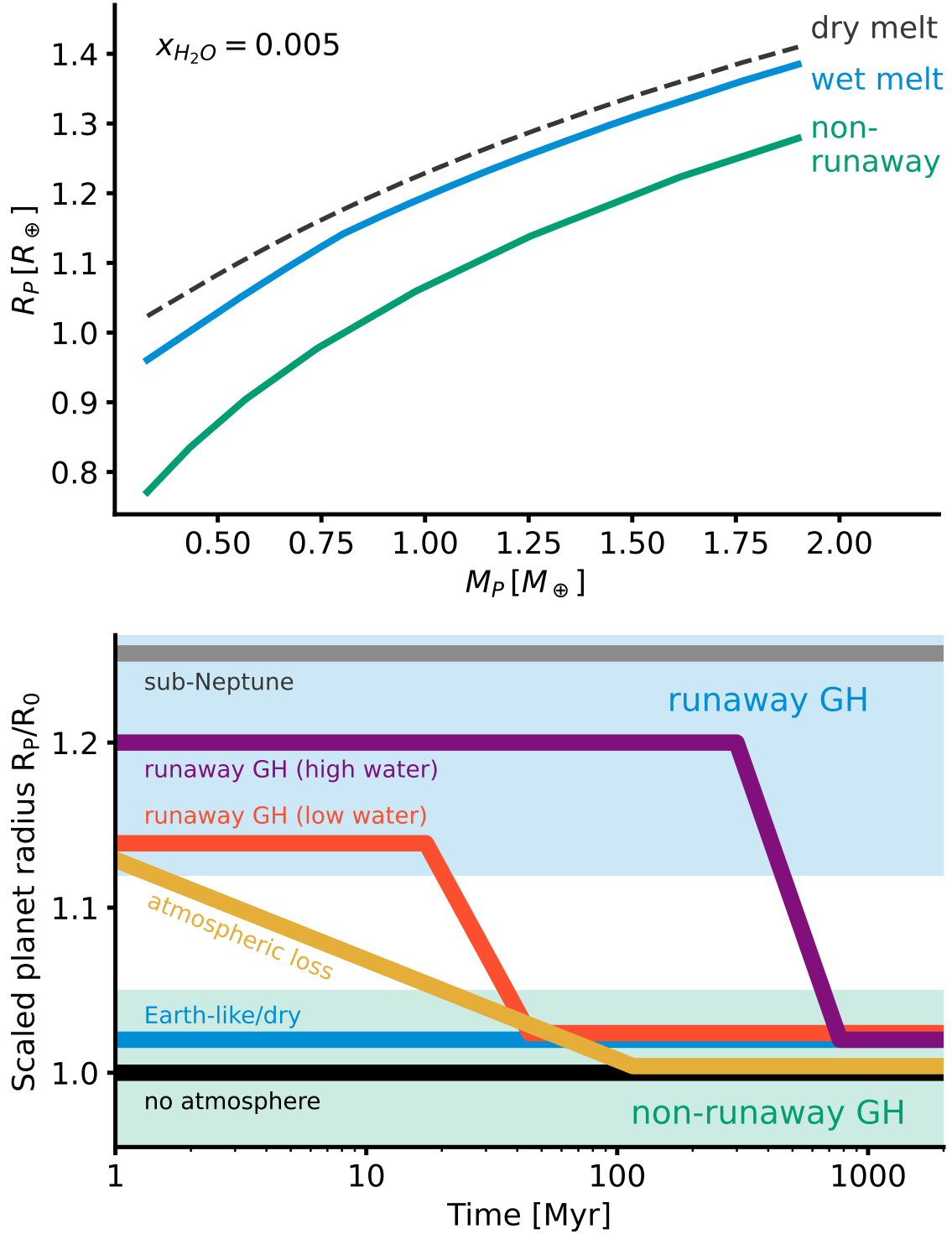


Figure 3. *Top:* Mass-radius relationships for a water mass fraction $x_{H_2O} = 0.005$ and different planet states. Green: planets with a solid mantle and no steam atmosphere. Dashed: planets with steam atmospheres. Blue: planets with steam atmospheres and including the effect of water incorporation in the melt. *Bottom:* Radius evolution of different planet types, illustrating degeneracies and potential for confusion among planet classes. Shown is a schematic time evolution of the transit radius normalized to the atmosphere-free radius R_0 for different scenarios. Planets can move between planet classes through processes such as atmospheric loss and desiccation, which ultimately ends a runaway greenhouse phase on a timescale dependent on a planet's water content.

that all planets receiving a net instellation $S < S_{\text{thresh}}$ follow the non-runaway greenhouse relation, and a fraction f_{rgh} of the planets with $S > S_{\text{thresh}}$ follow the wet melt relation. This parametrization introduces a discontinuity of average planet radii and bulk densities as a function of stellar irradiation. In the following, we test if and under what conditions this trend is large enough to be detected with high significance.

2.2. Survey simulations

The survey module of Bioverse converts the synthetic planet sample into a set of uncertainty-laden measurements on a subset of that sample. This task includes selection of the targets, application of detection biases, and conducting simulated measurements. All of the above are specific to the particular survey.

2.2.1. Detection bias and sample selection

Not all transiting planets are detectable with the same likelihood and detection biases have an impact on the demographic measurements we are interested in. A detailed characterization of the detection biases of individual missions would not be justifiable given the uncertainties of the theoretical predictions. Instead, we derived generic observing limits that reflect the limitations of state-of-the-art transit surveys.

The runaway greenhouse transition is expected to occur at orbits sufficiently close to let mission duration not be a limiting factor: S_{thresh} occurs close to Earth’s orbital period for G-type stars and on significantly shorter periods for the more prevalent M dwarf hosts (Goldblatt & Watson 2012). However, for a transit signal to be detected in a transit survey, it must reach a sufficient signal-to-noise ratio (S/N). This S/N is sensitive on the photometric precision that can be achieved (e.g., Burke et al. 2015; Hardegree-Ullman et al. 2019). In its in-orbit commissioning phase, the *CHEOPS* mission demonstrated a photometric precision of 75 ppm for faint ($V \approx 12$) stars (Benz et al. 2021). In comparison, *PLATO*’s expected precision for similar stars was estimated to be ~ 50 ppm (ESA 2017, Matuszewski et al., in prep.). To represent these photometric limits, we chose a minimum transit depth of 75 ppm as a detection limit and consider only measurements of planets exceeding this threshold. We further exclude target stars with *Gaia* magnitudes $M_G > 11$.

The runaway greenhouse effect becomes obsolete where no atmosphere can be maintained due to proximity to the host star and resulting atmospheric erosion. Ensuring to stay well clear of such regions, we clear our sample from all planets with a net instellation $S > 2000 \text{ W m}^{-2}$. We further consider only rocky planets with masses below $2 M_{\oplus}$.

2.3. Hypothesis tests

We now turn to assessing the simulated surveys in terms of their ability to detect the runaway greenhouse transition and their constraining power on parameters of this trend. To do this, we rely on a Bayesian hypothesis testing approach where we quantify the evidence of a hypothesis over another based on the (simulated) data.

For our specific problem, this implies comparing evidences for a demographic imprint of the runaway greenhouse effect to its absence.

2.3.1. Definition of the runaway greenhouse hypothesis

As a null hypothesis, we consider the case where the planetary radius distribution is independent of the instellation,

$$H_0(\theta, S) = \theta, \quad (4)$$

where θ is the set of parameters defining the radius distribution. We further define an alternative hypothesis that describes radius changes due to steam atmospheres and water in the melt. As motivated above, this hypothesis takes the form of a step function in net instellation S , where the step occurs at the outer edge of the runaway greenhouse region. Our main observable shall be the average planet radius in the planet population inside and outside this threshold. The runaway greenhouse hypothesis is then defined as

$$H_{\text{rgh}}(\theta, S) = \begin{cases} H_0, & S \leq S_{\text{thresh}} \\ \langle R_{\text{P}} \rangle (f_{\text{rgh}}, \Delta R_{\text{stm}}, \Delta R_{\text{wtr}}), & S > S_{\text{thresh}}. \end{cases} \quad (5)$$

Here, f_{rgh} is the fraction of planets experiencing a runaway greenhouse effect. ΔR_{stm} and ΔR_{wtr} are predicted radius changes from the steam atmosphere and water incorporation models, respectively. They are assumed to act additively on the planet radii and thus on their average $\langle R_{\text{P}} \rangle$.

The only free parameter of the null hypothesis, which assumes the average radius to be independent of instellation, is the predicted mean radius $\langle R_{\text{P}} \rangle$. The functional form of the runaway greenhouse hypothesis is more complex: Besides the mean radius of planets outside the threshold $\langle R_{\text{P}} \rangle_{\text{out}}$, which is a nuisance parameter necessary to define the hypothesis, it relies on the threshold instellation for the “step” S_{thresh} , the planetary water mass fraction $x_{\text{H}_2\text{O}}$, and the dilution factor f_{rgh} .

The measured radii $R_{\text{P},i}$ cannot be directly used for the hypothesis tests as they include intrinsic scatter that is not caused by measurement errors. H_{rgh} and H_0 should thus be tested against a statistical estimator that represents the population mean. To avoid binning and the artificial patterns it may introduce, we chose to test our hypotheses against a simple moving average *SMA* along the instellation axis with a window of size 25 centered around each measurement. We further computed the uncertainty of this moving average by propagating the individual measurement errors and applying a rolling standard error of the mean.

specify error propagation

As our procedure involves random sampling of the model parameters θ , we need to define the probability of obtaining a dataset given the model parameters, i.e., a likelihood function. We assumed here that the individual moving averages SMA_i

are measured with a normally distributed uncertainty σ_{SMA_i} and adopted a normal distribution

$$\mathcal{L}(SMA | \boldsymbol{\theta}) = \prod_i^N \frac{1}{\sqrt{2\pi\sigma_{SMA_i}^2}} \exp\left(-\frac{(SMA_i - H(\boldsymbol{\theta}, S_i))^2}{2\sigma_{SMA_i}^2}\right). \quad (6)$$

Here, $H(\boldsymbol{\theta}, S_i)$ corresponds to the functional form of the runaway greenhouse or null hypothesis.

2.3.2. Bayesian model comparison

We are now ready to assess the relative plausibility of H_{rgh} and H_0 given the synthetic data we have generated, assigning equal a priori probabilities to these models. This is done by comparing the Bayesian evidence \mathcal{Z} of the models, which we estimate with the nested sampling (Skilling 2004) algorithm *dynesty* (Speagle 2020). Our criterion to reject the null hypothesis is

$$\Delta \ln \mathcal{Z} = \ln \mathcal{Z}_{\text{rgh}} - \ln \mathcal{Z}_0 > 3. \quad (7)$$

A sensible choice of priors is central for evidence estimation via nested sampling. As the parameters we are interested in recovering, S_{thresh} and x_{H_2O} , are poorly constrained by previous data, we used relatively uninformative priors to sample the entire physically plausible parameter space. For S_{thresh} , we chose a uniform prior in $[10, 1000] \text{ W m}^{-2}$. We sample x_{H_2O} from a log-uniform distribution to imply scale-invariant ignorance. Its boundaries $[10^{-5}, 0.1]$ are motivated by the water mass fractions covered by the geophysical models (Sect. 2.1.6). Finally, we adopt a broad, uniform prior for $\langle R_P \rangle_{\text{out}}$ bound by $[0.1, 15] R_{\oplus}$. We then ran the nested sampler to compute the evidence and sample the posterior distributions.

3. RESULTS

3.1. Statistical signature of the runaway greenhouse threshold

To characterize the population-level imprint of individual radius changes, we generated a generic planet population with an injected runaway greenhouse effect assuming a water fraction $x_{H_2O} = 0.005$. Figure 4 shows the resulting planetary radii. When ordered in orbital period space, the different planet types overlap, diluting the demographic imprint. With net instellation as an independent variable, planets above and below the runaway greenhouse threshold separate. We also show the predictions of observable average planet radii from the statistical hypotheses defined above. Within the runaway greenhouse regime, an average radius change of 15% occurs.

3.2. Testability of the runaway greenhouse hypothesis

Figure 5 shows a prototypical statistical detection of the runaway greenhouse transition. For the sake of clarity, we chose an optimistic scenario where the sample of characterized planets is large ($N = 481$) and the measurement uncertainties are

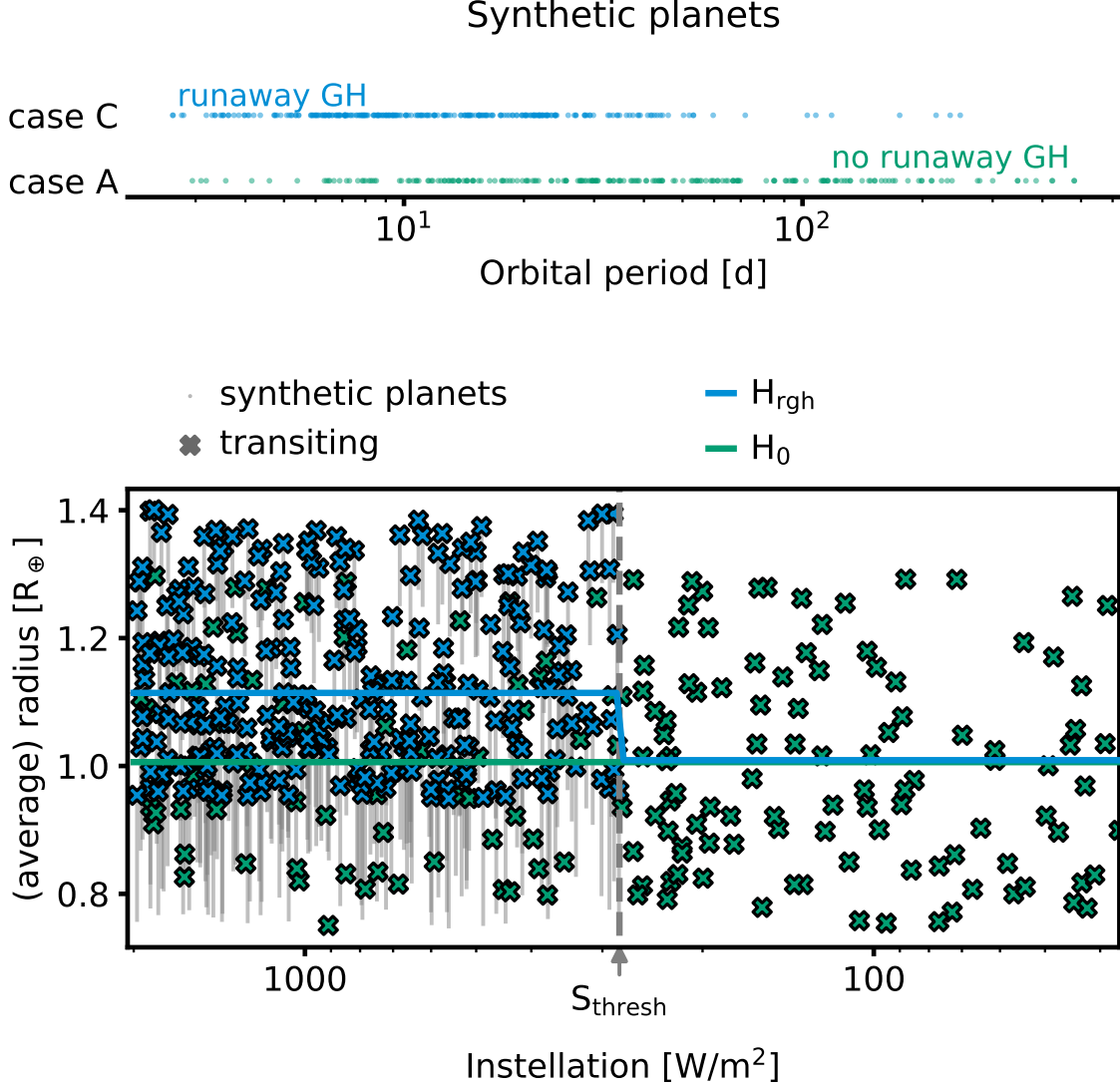


Figure 4. Synthetic planets above and below the runaway greenhouse threshold. *Top:* Planet state as a function of orbital period. Planets with and without a runaway greenhouse climate mix and are not distinguishable in period space. *Bottom:* Radii of synthetic planets with injected radius deviation as a function of net instellation. Only the planets marked as transiting are observable. Above the runaway greenhouse threshold $S_{\text{thresh}} = 280 \text{ W m}^{-2}$, the radii of a fraction of planets are inflated by the amount indicated with gray lines. The sharp boundary at S_{thresh} causes a discontinuity in the average planet radius (blue). This runaway greenhouse hypothesis can be tested against the null hypothesis H_0 (green), where average radii are independent of instellation.

small ($\sigma_R = 2\%$, $\sigma_S = 5\%$). We assumed that the fraction of those planets irradiated stronger than S_{thresh} that have runaway greenhouse climates is 0.8, and we chose a water mass fraction of 0.005 for each planet. In this case, the pattern was detected with high significance ($\Delta \ln \mathcal{Z} \approx 100$).

With such a strong signal, we can attempt an inference of the parameters defining the injected effect. Figure 6 shows the posterior distributions of S_{thresh} , x_{H_2O} , and f_{rgh} as determined by the nested sampler. The threshold instellation can be accurately

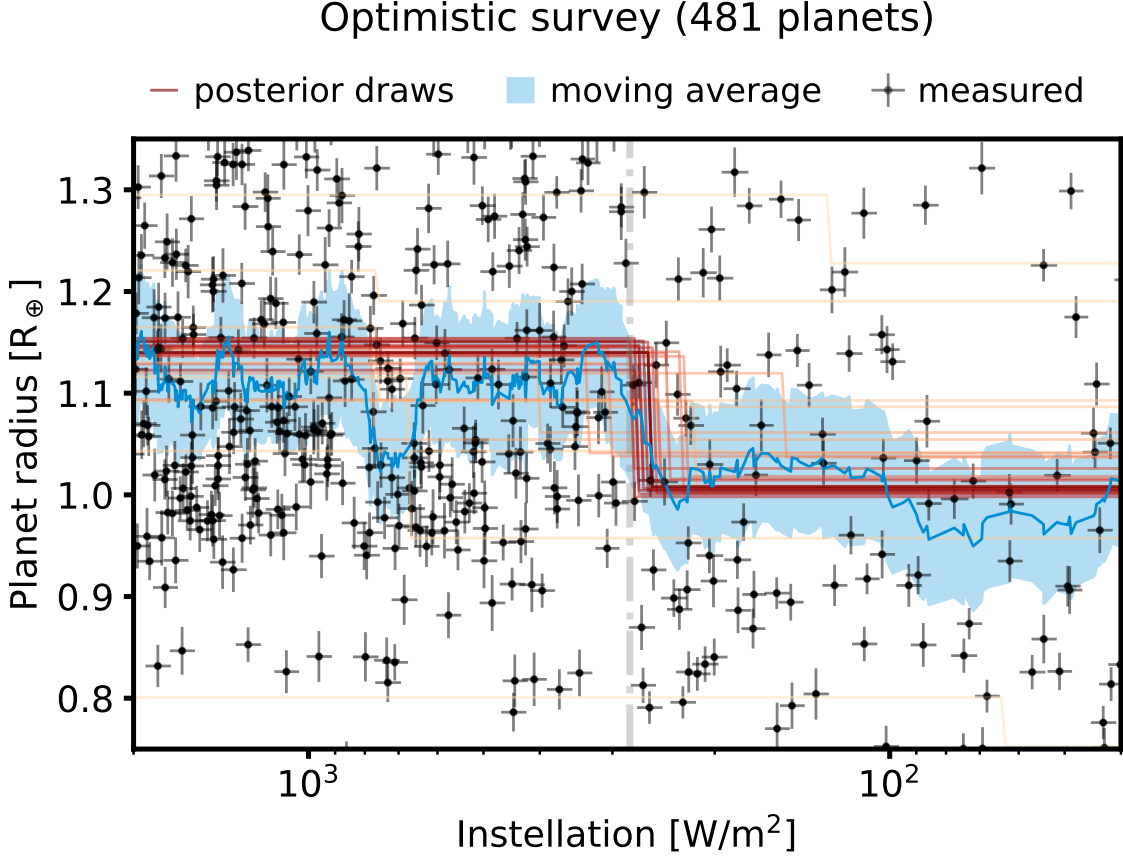


Figure 5. Detection of the runaway greenhouse threshold in the optimistic case. From simulated radius and instellation measurements of a large ($N = 481$) survey, we compute the moving average (blue confidence intervals) and fit the runaway greenhouse hypothesis to it (Eqn. 5, random draws from the posterior in red). The pattern is detected with high significance.

constrained with a median $\hat{S}_{\text{thresh}} = 276 \text{ W m}^{-2}$. Both a higher water mass fraction and a higher dilution factor lead to larger average radii, thus these parameters are strongly correlated.

Figure 7 explores the statistical power achieved in the above scenario for different combinations of the poorly constrained parameters x_{H_2O} and f_{rgh} . It is highest for large water inventories and large dilution factors. For all but very low water fractions, f_{rgh} dominates this trend: It enters linearly into the average planet radius, whereas the contribution of x_{H_2O} - as predicted by the geophysical models - is sublinear with a power-law exponent of ~ 0.3 . As long as f_{rgh} is larger than ~ 0.2 , a sample size of 481 is sufficient for a 50% detection rate even for water ratios as low as 10^{-3} .

3.3. Detecting the runaway greenhouse transition with current and planned exoplanet missions

Under real-world conditions, the planetary properties in question can only be probed with a finite precision that is specific to each exoplanet mission. *PLATO* (PLANetary

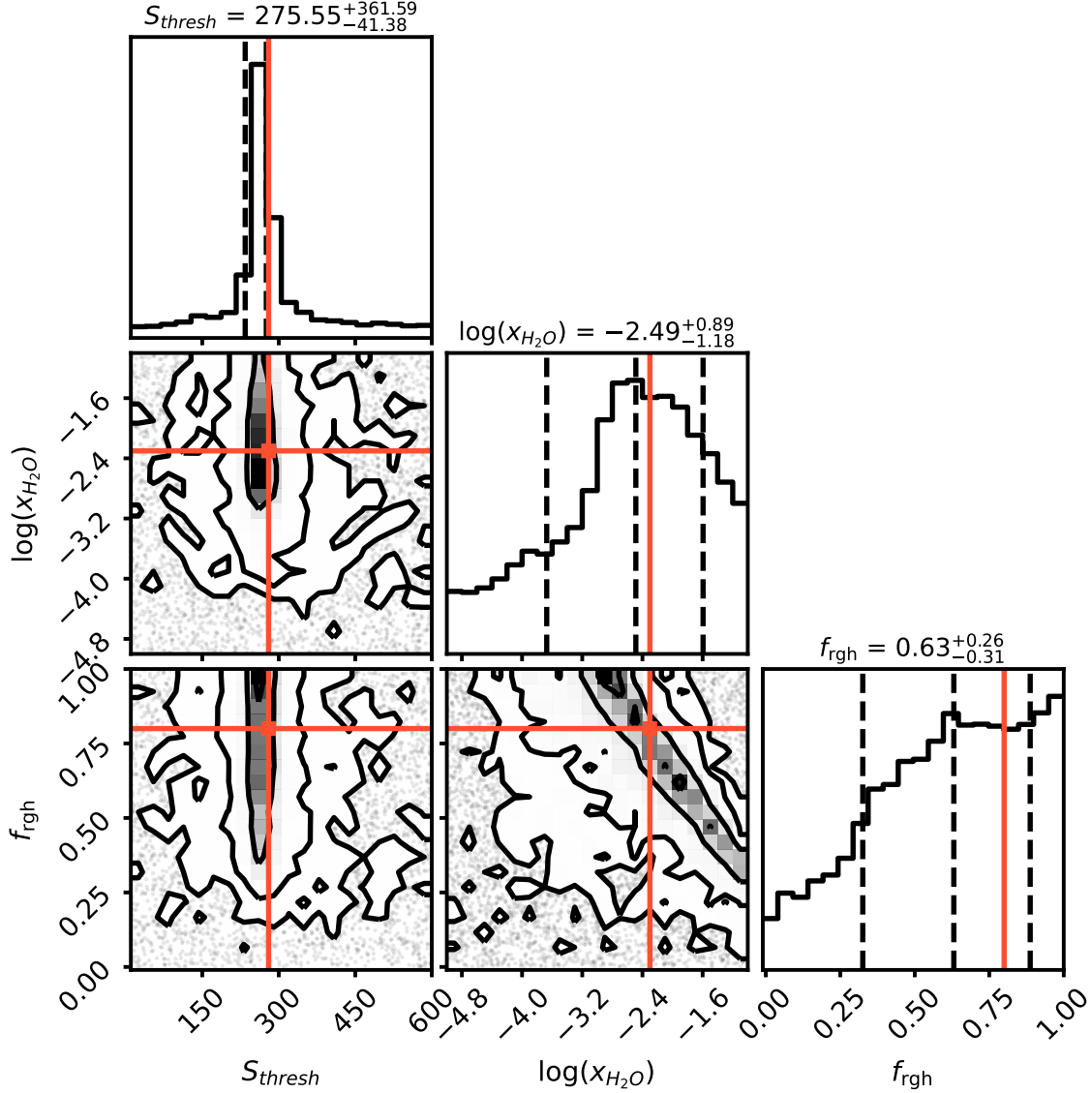


Figure 6. Retrieved posterior distribution of key parameters in the optimistic scenario. The density maps in each panel show relationships between and marginalized distributions of the model parameters as they could be retrieved with a high-precision transit survey and a sample of 481 planets. True values of the parameters for the injected effect are shown in orange. The threshold instellation can be reasonably constrained; the predominant water fraction and the fraction of planets with runaway greenhouse climates are degenerate.

Transits and Oscillation of stars) is an ESA mission designed to characterize terrestrial planets in the habitable zones of Sun-like stars, a goal to be achieved via long-term high-precision photometric monitoring of a sample of bright stars (Rauer et al. 2016). The *PLATO* team has released an estimate on the number of exoplanets that will be characterized in the course of the main survey mission (Matuszewski, priv. comm.). In the FGK sample of the mission, several hundred Earth-sized ($0.8\text{--}1.25 R_{\oplus}$) planets are expected to be detected. *PLATO*’s definition study report (ESA 2017) further states precision requirements for planet radii (3%), planet masses through radial

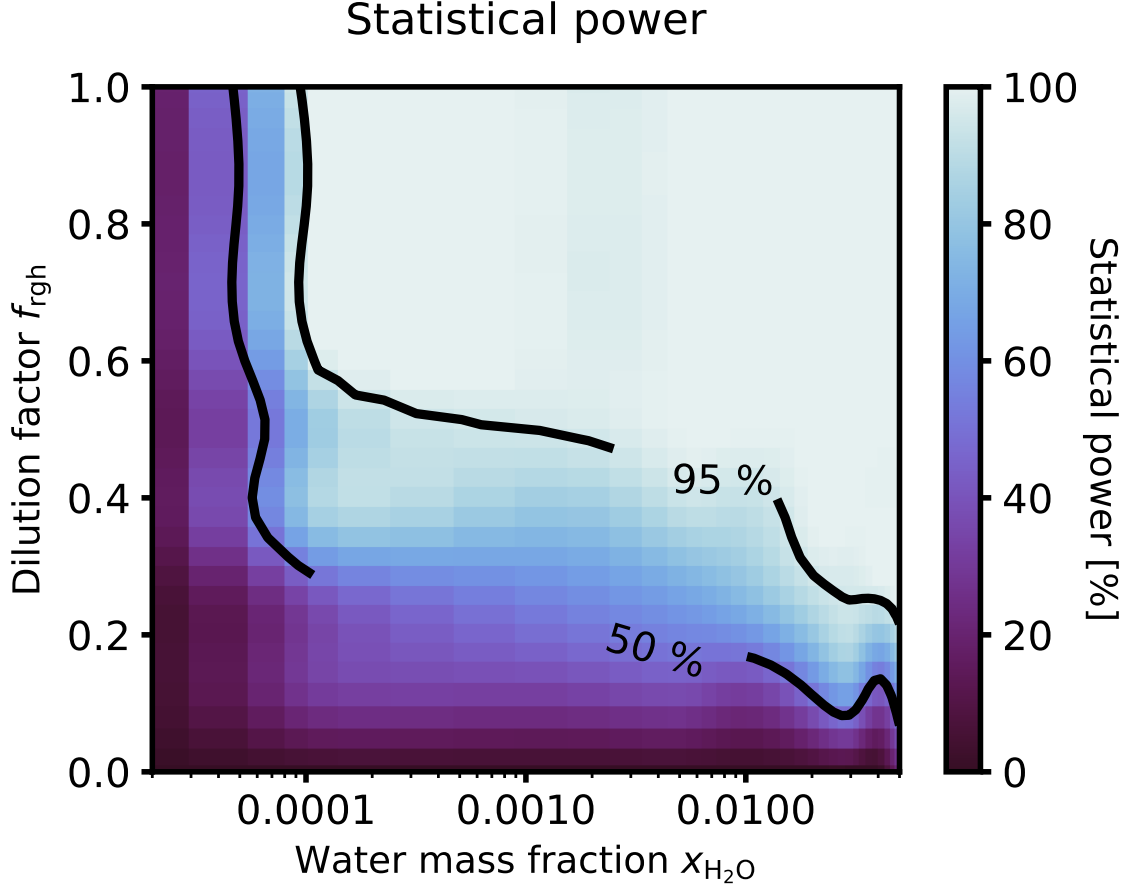


Figure 7. Statistical power of the runaway greenhouse hypothesis test as a function of model parameters. For a sample size $N = 481$, the color code shows the fraction of simulations resulting in a sound detection ($\Delta \ln \mathcal{Z} > 3$) for different combinations of water mass fraction and dilution factor. Higher values in either parameter result in a more reliable detection. For water mass fractions $\gtrsim 10^{-4}$, the statistical power largely depends on the fraction of greenhouse climate planets in the sample.

velocity (RV) follow-up (10%), and stellar masses, radii, and ages (10%). We base our assessment of *PLATO*'s diagnostic power on these estimates.

For a volume-limited sample, considering all host star spectral types, we find that a yield of 270 planets enables a significant detection if the fraction of runaway greenhouse planets is larger than ~ 0.1 (see Fig. 8). The minimum needed fraction rises to 0.3 for $N = 100$. For much smaller samples, even an optimistically strong signal can no longer be detected.

What other planned missions are suited to test the runaway greenhouse hypothesis? The ongoing *CHEOPS* mission was designed as a follow-up mission to search for transits of planets discovered with other techniques, in particular with radial velocity measurements (Benz et al. 2021). As such, it will provide precise radius constraints on a sample of small planets; however, only a small number of planets with periods

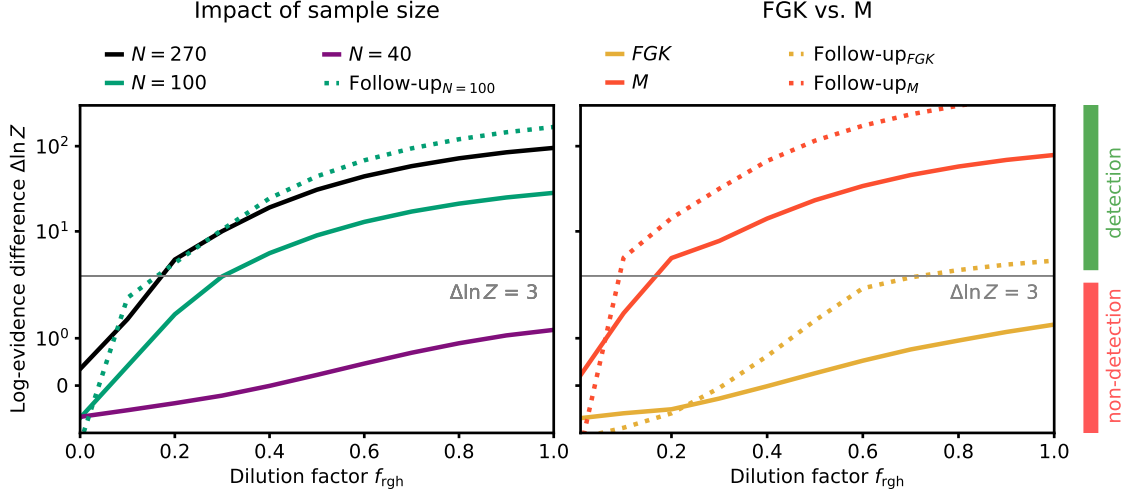


Figure 8. Expected delta-evidences as a function of the fraction of planets having runaway greenhouse climates for different versions of the *PLATO* survey. The median values of randomized survey simulations are shown; $\Delta \ln Z > 3$ (gray horizontal line) is considered sufficient evidence to reject the null hypothesis. *Left:* For a large planet yield of $N = 270$, even small dilution factors ~ 0.1 allow a detection. A sample of 100 planets is sufficient if their masses are constrained to within 10% (dotted green line). Without such follow-up measurements, sufficient diagnostic power can only be achieved with this sample if $f_{\text{rgh}} \gtrsim 0.3$. Even smaller samples are unlikely to yield a significant detection. *Right:* Evidences when only FGK or only M dwarfs are considered. Only M dwarfs host enough planets on both sides of the threshold instellation to allow a reliable detection of the runaway greenhouse signal.

>50 d are being observed. This largely limits *CHEOPS*’ coverage to planets within the runaway greenhouse regime, preventing a detection of the transition.

As *CHEOPS*, *Ariel* (Puig et al. 2016) will be a follow-up mission that is not designed to provide a large number of new radius measurements. *Ariel*’s primary targets are larger planets in the range of sub-Neptune to Jupiter-like planets. We thus do not expect a significant contribution to exploring the inner edge of the habitable zone for Earth-sized planets.

While not primarily designed to detect transiting planets, the *Nancy Grace Roman Space Telescope* (Spergel et al. 2015) is expected to yield $\sim 10^5$ transiting planets on short orbits and constrain their radii in the course of its mission (Montet et al. 2017). In a fraction of the cases, planets as small as $2 R_{\oplus}$ will be detected. About 200 planets smaller than Neptune are expected to be found around M dwarfs and thus may reach into the habitable zone. The *Nancy Grace Roman Space Telescope* could thus provide a useful sample to explore the runaway greenhouse transition, albeit with a predominant focus on water-rich (sub-)Neptunes (e.g., Pierrehumbert 2022).

3.4. Statistical power of different mission designs

To explore the impact of mission trade-offs on the detectability of the runaway greenhouse transition, we simulated several transit surveys with different designs and strategies and measured their capability to recover the trend and constrain its pa-

rameters. We assessed this capability based on two determinants: the likelihood that the mission is able to detect the injected trend, and the precision with which it can constrain the parameters of that trend.

3.4.1. Additional planet mass measurements

The dependencies of a detection change when additional information beyond planet radii is available for the characterized planet population. Since the planet bulk density $\rho \propto R^{-3}$, the signal is stronger when measured in bulk density instead of radius: With an optimistic choice of geophysical parameters (see above), the average measured radius change is 15% whereas the average density change is -33% . Constraining bulk densities requires planetary mass measurements. We now examine the value of a follow-up campaign to constrain planet masses with respect to the detectability of the runaway greenhouse threshold.

For uncertainties in density measurements, we propagate normally distributed errors of mass measurements assuming $\sigma_{M_p} = 10\%$, as expected for *PLATO*. As can be seen in Fig. 8, the detectability is enhanced when radius constraints can be augmented with mass measurements: At unchanged sample size, the difference in Bayesian evidence can be up to an order of magnitude larger. Consequently, we achieve a statistically significant detection with smaller samples or lower dilution factors f_{rgh} . A density-based survey of 100 targets is roughly equivalent to a radius-based survey of 270 targets. At $N = 100$, pure radius measurements require $f_{\text{rgh}} \gtrsim 0.4$ whereas bulk density measurements enable a detection from $f_{\text{rgh}} \gtrsim 0.1$.

3.4.2. Spectral type of target stars

Since receiving radiation is sensitive on the spectral type of the host star, the share of planets on either side of S_{thresh} is different for FGK and M dwarfs. We tested the detectability of the runaway greenhouse signal when only FGK or only M dwarfs are considered (see Fig. 8). The samples are volume and magnitude-limited to reflect the target counts of *PLATO*'s provisional Long-duration Observation Phase fields (15996 FGK stars in the P1 and P2 samples, 33948 M stars in the P4 sample, [Nascimbeni et al. 2022](#)). The resulting M dwarf planet sample is significantly larger with 219 ± 13 planets compared to 40 ± 6 planets in the FGK sample. No significant detection is possible in the pure FGK sample, independent of the assumed geophysical parameters. In the M dwarf sample, the evidence threshold is reached around $f_{\text{rgh}} \sim 0.2$, similar to the case above where all spectral types are considered.

3.4.3. Constraining the threshold instellation

A key constraint resulting from a successful detection is a measurement of S_{thresh} . Here, we assess the ability of different mission concepts explored above to constrain this parameter. Figure 9 shows posterior distributions from a grid of inferences together with the true values of the injected signal for different fractions f_{rgh} . We consider three cases: only radius measurements, radius and mass measurements, and

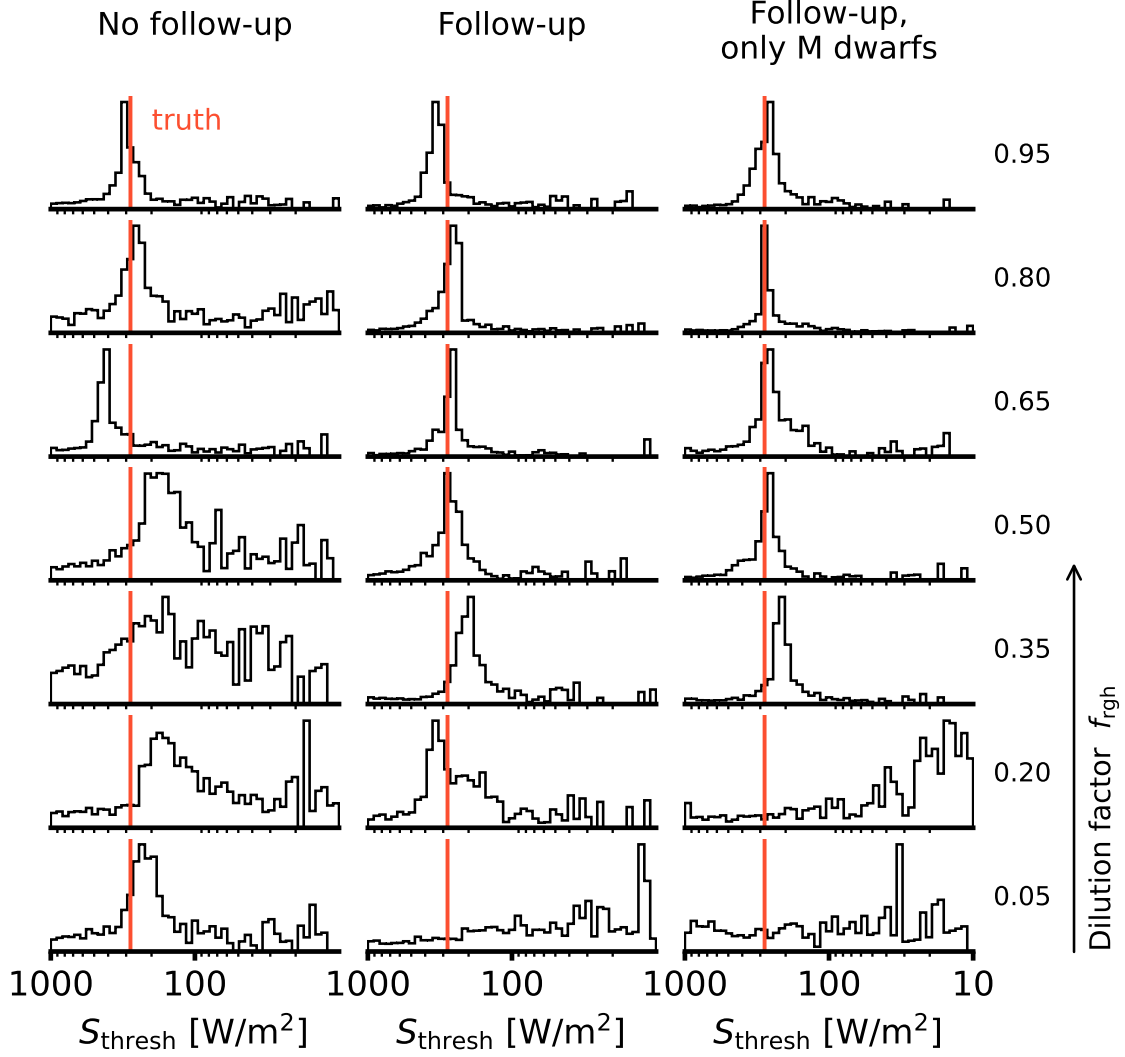


Figure 9. Retrieved posterior distributions of the threshold installation for different survey realizations. All cases assume $x_{H_2O} = 0.005$ and a planet sample size $N = 100 \pm 10$; The fraction of planets with runaway greenhouse climates varies across rows. Orange lines show the true value of the injected signal. Accuracy and precision of the constraint on S_{thresh} generally improve with higher f_{rgh} . Bulk density-based inferences improve the constraints, and M dwarf samples yield the highest accuracy.

radius and mass measurements of only planets orbiting M dwarfs. The simulations otherwise represent the simulated PLATO example described above. We chose a planetary sample size of $N = 100 \pm 10$, as this was found to be a threshold case in Sect. 3.3.

Accurate retrievals from radius measurements alone require high fractions of greenhouse climate-bearing planets to achieve an accurate constraint on S_{thresh} . If, on the other hand, a follow-up campaign adds planetary mass estimates and we fit the signal in bulk density space, useful constraints are possible under more pessimistic conditions. A sample containing only planets around M dwarf yields a comparable performance as the overall sample.

4. DISCUSSION

Potential discussion points:

(How close is Earth to runaway? (-> Goldblatt & Watson (2012); Popp et al. (2016); what is the max. expected change in Earth's albedo due to deglaciation?)

Caveats: see Turbet et al. (2019) Sect. 3, Bower et al. (2019). Mention we only consider instellation-induced rgh.

- we ignore water loss by H₂O photolysis in the upper atmosphere and subsequent H escape, which would eventually cool even planets within the runaway greenhouse regime (Lichtenberg et al. 2022).

- we ignore tidal heating, which could extend the magma ocean phase of close-in planets (and change their orbits via tidal orbital evolution) (Jackson et al., 2008; Barnes et al., 2013 (?)).

- assumption of a single albedo. "if there is a range of albedos, will that wash away the signal?" - Impact of assumptions on findings, e.g. M-R relation. "We should have a discussion section dedicated to the impact of assumptions on the findings - including mass-radius. A good way to go about this is to present bracketing cases; or to discuss why the discontinuity in the results would not be affected by changes that led to continuous offsets in the results. Or both. But it should not be in the methods section."

4.1. Statistical imprint of exoplanet climates

The runaway greenhouse transition is a robust prediction from climate models, and its impact on planetary bulk properties has been shown to be in the detectable range of current astronomical instrumentation (Goldblatt 2015). Measuring these impacts would indeed provide the first empirical evidence of the habitable zone concept. On the planetary level, however, such undertaking is hindered by degeneracies: From internal composition to atmospheric loss to volatile content, many factors influence a planet's size. It is therefore prudent to shift the focus to the planet population as a whole and search for a statistical effect in exoplanet demographics (Turbet et al. 2019). Using Bioverse to combine the predictions from geophysical models of steam atmospheres with a synthesis of planets informed by observed demographics, we showed that the population of greenhouse-inflated planets create a signature in the radius and density distribution that is well in the detectable range.

However, the idealized step-function central to our hypothesis tests is blurred by several factors. Its amplitude is affected by "sub-Neptunes" with significant Hydrogen/Helium envelopes, which can disguise as inflated rocky planets. They might not contribute to the demographic signal we are looking for, although a similar transition was suggested for water-dominated sub-Neptunes (Pierrehumbert 2022). A subset of such gas-rich planets will experience atmospheric loss via photoevaporation (Owen & Wu 2013) or core-powered mass loss (Ginzburg et al. 2018), turning them from planets appearing inflated into much smaller (super-)Earths. Further dilution comes from the population of planets that lack an atmosphere or sufficient volatiles that can create a steam atmosphere. There is also a time dependence, both because stellar luminosities change with age and because runaway greenhouse planets with limited water reservoirs ultimately desiccate, ending their steam atmosphere phase. Intrinsic variation in the threshold instellation is caused by differences in planetary features influencing the onset of a runaway climate such as albedo, atmospheric composition, or surface gravity (Pierrehumbert 2022).

All of the above mechanisms dilute the demographic imprint of the runaway greenhouse transition with contributions that are challenging to quantify. The "dilution factor" we introduced embodies our ignorance of these contributions. Importantly, while this may offset our estimates of the signal's amplitude, its shape remains the same.

Our finding that the expected trend is strong except for extremely low water mass fractions not only gives reason for optimism regarding its detection, it also presents a

potential for constraints on the water inventory of terrestrial planets in the case of a non-detection. Should a successful detection occur, the time dependencies discussed above should be taken into account when using this population-level information to constrain exoplanet climates.

4.2. Detectability of the runaway greenhouse transition

the demographic imprint is detectable. Under what conditions?
Mention multiplanet systems.

We showed in Sect. 3.2 that under favorable conditions, a sufficiently large (481 planets) photometric survey is likely to detect the demographic imprint of the runaway greenhouse transition and accurately constrain the associated threshold instellation. However, even assuming capable instrumentation and an optimal survey design, geophysical and demographic unknowns may jeopardize this undertaking. The detectability of the runaway greenhouse threshold is thus a function of both survey design and astrophysical circumstances.

4.2.1. Key factors influencing tests of the runaway greenhouse hypothesis

What influences the probability of correctly rejecting a false null hypothesis? We identified the following drivers of the diagnostic power for detecting the runaway greenhouse transition with a transit survey:

avoid bullet points within sub-subsections

- Occurrence rate of planets forming steam atmospheres: The runaway greenhouse climate relies on the production of large amounts of water vapor that then acts as a greenhouse gas. This process works only on planets with an atmosphere and of sufficiently volatile-rich composition

TIM: how much?

- . The fraction of planets fulfilling these requirements has an impact on the amplitude of the demographic imprint of the runaway greenhouse transition.
- Planetary evolution and duration of the steam atmosphere phase: An inflated steam atmosphere can only be sustained until the planet has lost its water. Depending on host star spectral type, planetary mass, and composition, planets can spend from a few Myr to several Gyr in runaway greenhouse climates (Hamano et al. 2015; Luger & Barnes 2015), and only planets observed during this phase will contribute to the signal.
- Prevalent water inventory: The magnitude of radius change at the runaway greenhouse threshold is sensitive on the water mass fraction. As a result, the statistical abundance of water in terrestrial planets impacts the strength of the demographic pattern: The higher the water content and the higher the fraction of planets in runaway greenhouse climates, the greater the prospect of a statistically sound detection.

- Sample size: Since we are looking for a population-level trend, the statistical significance increases with a larger sample size.
- Radius measurement precision: The more precise individual planet radii can be determined, the less smeared out the pattern will be. Good *accuracy* is less important, as long as it does not have a systematic error scaling with stellar irradiance.
- Availability and precision of mass measurements: For simple geometric reasons ($\rho \propto R^{-3}$), the expected trend is stronger when measured in bulk density than it is in planet radius space. If transiting planets can be followed up to obtain mass measurements, the statistical significance increases.

Besides these main factors, uncertainties in the measured instellations can influence the result, although they are typically small due to the very precise orbital period measurements available for transiting planets. This can be different for young host stars when their ages can not be well constrained; in particular the long pre-main sequence phase of M dwarfs shows a large variation in bolometric luminosity (see Fig. 2).

4.2.2. *False positive scenarios*

what other processes could be confused with a magma ocean signal?
If there's no other subsection here, make this a (the final?) subsection in "Discussion".

Runaway greenhouse climates are not the only physical mechanism that may cause a change in transit radius for a subset of planets. Some of the most prominent alternative scenarios involve atmospheric loss due to either photoevaporation through high-energy radiation by the host star (e.g., Owen & Wu 2013; Jin et al. 2014; Mordasini 2020) or due to residual heat from the planet's interior shortly after formation (Ginzburg et al. 2016, 2018; Gupta & Schlichting 2019). Both processes are being traded as potentially sculpting the observed bimodality in the radius distribution of small exoplanets (Fulton et al. 2017; Van Eylen et al. 2018). Either of them leads to a decrease of planet radius for planets close to their host star, which is distinct from the radius inflation introduced by runaway greenhouse climates.

Another false positive contribution may come from potential unknown variations in the occurrence rate gradients in radius-instellation space. They can impact the statistical inference of the transitions, especially if these variations are similar to the expected pattern. Although an abrupt pattern at the expected runaway greenhouse transition seems unlikely, examples of steep occurrence rate density changes exist. An example is the "Neptune desert", a triangular region of low planet occurrence density of close-in planets in period-radius space (Szabó & Kiss 2011; Mazeh et al. 2016; Dreizler et al. 2020). The shape of this region is such that smaller planets become less frequent the closer to the star they are, which to some degree resembles the pattern introduced by the instellation dependency of the runaway greenhouse transition. However, the Neptune desert occurs at smaller orbital

periods and its location depends on a planet’s size (Szabó & Kiss 2011), which is not expected for the runaway greenhouse transition.

is there overlap/confusion with the radius/density trend in Luque & Pallé (2022)?

4.2.3. *OPTIONAL...: Atmospheric signatures*

discuss potential atmospheric signatures of magma oceans. e.g.: H/O ratios of sub-Neptunes could be low (because H is in the melt) (Tim’s talk)

“Can a smaller sample size’s diagnostic value be increased if atmospheric compositional information can be added, i.e., PLATO + ARIEL (or similar combo)?”

4.3. *Diagnostic power of near-future exoplanet missions*

The fidelity of a future detection or falsification of a runaway greenhouse signature will depend on the significance with which the null hypothesis can be excluded. As a consequence, instrumentation and survey strategy aiming at testing the hypothesis should aim at maximizing the probability of a true positive detection. In Sect. 3.3 we explore the diagnostic power of space missions that are currently operating or are in the planning stage. We focus here on transit survey missions, as they provide the most direct radius measurements of a practical planet sample.

As discussed above, the key drivers from a mission design perspective are sample size and photometric precision. We found that along these axes, *PLATO* will be the most favorable among the upcoming transit missions. With an expected transit radius precision of 3% (ESA 2017) and a yield of > 100 planets characterized with such high precision (Rauer 2021), *PLATO* is comparable to the optimistic survey we introduced in Sect. 3.2. If successful, it should readily detect the predicted statistical imprint or, in case of a non-detection, provide strong upper limits on the occurrence rate of runaway greenhouse planets.

The latter depends on the lifetimes of runaway greenhouse phases, which are a function of the initial water inventory of the planets (Hamano et al. 2015). It seems thus feasible to derive the typical water content of rocky planets from these occurrence estimates.

4.4. *Mission design trades*

not sure if subsubsections needed

We now turn to mission design trades that influence the statistical power for testing the runaway greenhouse hypothesis.

4.4.1. *The value of follow-up campaigns*

As runaway greenhouse phases leave a stronger imprint in bulk density than in planet radius (see Sect. 3.4.1), it would be beneficial to obtain constraints on planetary masses and test the runaway greenhouse hypothesis in density space instead of radius space. Precise ground-based radial velocity measurements are expensive, and therefore such follow-up efforts may only be available for a subsample of a mission’s targets. For a mission design similar to *PLATO*, a density-based test on about a third of the overall sample is equivalent to a pure radius-based analysis. The diagnostic power of such a test may be

improved by simultaneously fitting for the trend in radius space in the subsample without RV follow-up. An optimized mission in search for the inner edge of the habitable zone will further enhance its information content via a wise selection of follow-up targets, i.e., favoring those planets residing close to the expected instellation threshold S_{thresh} .

4.4.2. Target star spectral types

To date, the majority of planets with radius measurements orbit FGK dwarfs, and, based on the instellation they receive, most of them lie in the runaway greenhouse regime (Thompson et al. 2018). Obviously, a step-function-like signal in the exoplanet demographics like the one illustrated above can not be constrained well if only one side of the discontinuity is being sampled. This, however, is the situation for planetary systems around Sun-like stars – their habitable zones are so distant that transiting planets within them are very rare due to pure geometrical reasons. It was, among other reasons, the sharp drop in transit probability with orbital distance that has prompted a number of recent transit surveys to specifically target M dwarfs (e.g., Irwin et al. 2009; Obermeier et al. 2016; Delrez et al. 2018; Sebastian et al. 2021; Dietrich et al. 2023), but the sample of terrestrial planets orbiting them is still small (e.g., Berger et al. 2020; Hardegree-Ullman et al. 2020).

M dwarf systems are also key for detecting the runaway greenhouse transition: Our calculations with different spectral types (Sect. 3.4.2) show that the information content of M dwarfs in a sample dominates the hypothesis tests. Besides their large number in a volume/magnitude-limited sample, transiting M dwarf planets are more likely to be located near the threshold instellation and in particular beyond it, i.e., in the optimistic habitable zone. The transit depth difference at the transition is expected to be larger for M dwarfs (~ 100 ppm for early, ~ 1000 ppm for late M stars Turbet et al. 2019), enhancing the demographic signal it leaves. An additional advantage of targeting M dwarfs are their extended runaway greenhouse phases, whose duration can reach the order of 100 Myr (Luger & Barnes 2015). This increases the probability of observing any given planet in the sample during the runaway greenhouse phase, essentially driving f_{rgh} to higher values. Therefore, in addition to the high scientific value of boosted detections of potentially habitable planets, M dwarfs are also indispensable for the discovery and characterization of the runaway greenhouse transition. As with a pure volume-limited sample, a targeted M dwarf survey, too, profits from follow-up measurements of planetary masses with an order of magnitude increase in evidence.

4.5. Constraining planetary habitability

Magma oceans influence the amount of water available at the surface and atmosphere, which is 1. commonly used as environmental marker to assess habitability, and 2. influences the planet's climate (greenhouse effect).

A potential for liquid water on the surface of a planet is commonly used as an environmental marker to assess its habitability. REF The runaway greenhouse transition represents an upper bound on received irradiation for this condition. Its detection

would thus not only empirically confirm the habitable zone concept but also help to locate it in the observationally available planetary parameter space. In Sect. 3.4.3, we show that the threshold instellation at which the runaway greenhouse transition occurs can be reasonably constrained without imposing overly optimistic conditions on the underlying planet population, instrumentation, or survey strategy.

elaborate based on Sect. 3.4.3

The situation is different for the planetary water inventory and the fraction of planets with runaway greenhouse climates: Since these parameters are degenerate, they cannot be well constrained without independent measurements.

discuss additional measurements that could lift the degeneracy. e.g., adding atmospheric compositional information i.e., PLATO + ARIEL or similar

4.6. *Impact of assumptions on our findings*

4.6.1. *Baseline mass-radius relationship*

Our baseline mass-radius relationship assuming pure MgSiO_3 interiors (Zeng et al. 2016) might not be representative of the rocky planet population. However, while interior composition may change the magnitude of radius inflation and could introduce an offset to its demographic imprint, we do not expect a change of its structure. The magnitude of the radius inflation effect is in fact expected to be larger for an Earth-like interior composition with an iron core-silicate mantle structure.

TIM: do you have a reference for this statement?

We thus consider our mass-radius relationship a conservative case and do not expect a negative impact on the detectability of the runaway greenhouse transition due to deviations from it.

if feasible: run a test with a different M-R relation. do we expect that the choice of M-R relation impacts the results? Perhaps have an appendix section.

4.6.2. *Water mass fraction*

The predominant mass fractions of water, which sensitively controls the atmospheric state of a rocky exoplanet, is poorly constrained. Inferred water contents in the literature range from upper limits on the order 10^{-5} to “water worlds” with tens of percent weight fraction (e.g., Rogers & Seager 2010; Unterborn et al. 2018; ?; Agol et al. 2021; Luque & Pallé 2022), all of which are within the realm of theoretical predictions (Mulders et al. 2015; Sato et al. 2016; Jin & Mordasini 2018; Bitsch et al. 2019; ?; Emsenhuber et al. 2021; Schlecker et al. 2021). Our nominal case assumes a water mass fraction of $x_{\text{H}_2\text{O}} = 0.005$. This can be considered a conservative choice that is unlikely to introduce a systematic overestimation of the statistical radius inflation trend, also since the hypothesis tests are only marginally sensitive on $x_{\text{H}_2\text{O}}$ as long as it is $\gtrsim 10^{-4}$ (see Sect. 3.2). Cases of pure rocky composition and very low volatile contents can be considered absorbed by the dilution factor f_{rgh} . Assuming a distribution of water mass fractions instead of a fixed value would thus not significantly change our results.

5. CONCLUSIONS

Runaway greenhouse climates on rocky planets cause significant inflation of their radii. Using Bioverse, a quantitative hypothesis testing framework, we have explored the potential of contemporary exoplanet missions to statistically detect a radius discontinuity resulting from this inflation in the exoplanet population. Our key findings are as follows:

1. The predicted tipping point in planetary climates causes a discontinuity in the radius and density distribution of small exoplanets with respect to the incident host star irradiation.
2. The demographic imprint of the runaway greenhouse threshold should be detectable with high-precision transit measurements. For a large sample $\gtrsim 100$, a detection is likely if radius inflation occurs on at least 10% of the observed planets and if typical water mass fractions are above $\sim 10^{-3}$.
3. We find that the planned *PLATO* transit survey will provide a sufficient sample and the required precision to detect the predicted trend. Assuming the projected photometric precision, *PLATO* will be able to test the runaway greenhouse hypothesis for planet yields $\gtrsim 100$.
4. The diagnostic power of transit missions in testing this hypothesis can be increased through a follow-up campaign providing planet mass measurements. This can reduce the required planet yield by about a factor of three. An optimized survey will further focus on M dwarfs to ensure sufficient targets on both sides of the expected threshold instellation.
5. Testing the runaway greenhouse hypothesis will constrain the water inventory of rocky exoplanets, providing important context in the assessment of their habitability. A detection will provide an empirical confirmation of the habitable zone concept and localize its inner edge.

The habitable zone is widely employed in target prioritization for exoplanet missions, and it will provide context for interpreting potential signatures of life. As we have demonstrated, it appears realistic that an empirical confirmation of the habitable zone concept is imminent. This will be a key contribution to the search for extraterrestrial life in the Universe.

Author contributions:

DATA AVAILABILITY

All data sets and software required to reproduce our results and this article are available through GitHub and Zenodo. The code to reproduce the figures can be accessed via the icon links associated with the respective figure caption.

Software: Bioverse (Bixel & Apai 2021), Astropy (Astropy Collaboration et al. 2018), NumPy (Harris et al. 2020), SciPy (Virtanen et al. 2020), corner.py (Foreman-Mackey 2016), dynesty (Speagle 2020).

REFERENCES

- Abe, Y., & Matsui, T. 1988, *Journal of the Atmospheric Sciences*, 45, 3081, doi: [10.1175/1520-0469\(1988\)045<3081:EOAIGH>2.0.CO;2](https://doi.org/10.1175/1520-0469(1988)045<3081:EOAIGH>2.0.CO;2)
- Adams, F. C., Bodenheimer, P., & Laughlin, G. 2005, *Astronomische Nachrichten*, 326, 913, doi: [10.1002/asna.200510440](https://doi.org/10.1002/asna.200510440)
- Agol, E., Dorn, C., Grimm, S. L., et al. 2021, *The Planetary Science Journal*, 2, 1, doi: [10.3847/PSJ/abd022](https://doi.org/10.3847/PSJ/abd022)
- Astropy Collaboration, Price-Whelan, A. M., Sipőcz, B. M., et al. 2018, *The Astronomical Journal*, 156, 123, doi: [10.3847/1538-3881/aabc4f](https://doi.org/10.3847/1538-3881/aabc4f)
- Baraffe, I., Chabrier, G., Allard, F., & Hauschildt, P. H. 1998, *Astronomy and Astrophysics*, v.337, p.403-412 (1998), 337, 403
- Barnes, J. W. 2007, *Publications of the Astronomical Society of the Pacific*, 119, 986, doi: [10.1086/522039](https://doi.org/10.1086/522039)
- Barnes, R., Mullins, K., Goldblatt, C., et al. 2013, *Astrobiology*, 13, 225, doi: [10.1089/ast.2012.0851](https://doi.org/10.1089/ast.2012.0851)
- Barth, P., Carone, L., Barnes, R., et al. 2021, *Astrobiology*, 21, 1325, doi: [10.1089/ast.2020.2277](https://doi.org/10.1089/ast.2020.2277)
- Benz, W., Broeg, C., Fortier, A., et al. 2021, *Experimental Astronomy*, 51, 109, doi: [10.1007/s10686-020-09679-4](https://doi.org/10.1007/s10686-020-09679-4)
- Berger, T. A., Huber, D., Gaidos, E., van Saders, J. L., & Weiss, L. M. 2020, *The Astronomical Journal*, 160, 108, doi: [10.3847/1538-3881/aba18a](https://doi.org/10.3847/1538-3881/aba18a)
- Bergsten, G. J., Pascucci, I., Mulders, G. D., Fernandes, R. B., & Koskinen, T. T. 2022, *The Demographics of Kepler’s Earths and Super-Earths into the Habitable Zone*
- Bitsch, B., Raymond, S. N., & Izidoro, A. 2019, *Astronomy & Astrophysics*, 624, A109, doi: [10.1051/0004-6361/201935007](https://doi.org/10.1051/0004-6361/201935007)
- Bixel, A., & Apai, D. 2020, *The Astrophysical Journal*, 896, 131, doi: [10.3847/1538-4357/ab8fad](https://doi.org/10.3847/1538-4357/ab8fad)
- . 2021, *The Astronomical Journal*, 161, 228, doi: [10.3847/1538-3881/abe042](https://doi.org/10.3847/1538-3881/abe042)
- Boukrouche, R., Lichtenberg, T., & Pierrehumbert, R. T. 2021, *The Astrophysical Journal*, 919, 130, doi: [10.3847/1538-4357/ac1345](https://doi.org/10.3847/1538-4357/ac1345)
- Bower, D. J., Kitzmann, D., Wolf, A. S., et al. 2019, *Astronomy & Astrophysics*, 631, A103, doi: [10.1051/0004-6361/201935710](https://doi.org/10.1051/0004-6361/201935710)
- Burke, C. J., Christiansen, J. L., Mullally, F., et al. 2015, *The Astrophysical Journal*, 809, 8, doi: [10.1088/0004-637X/809/1/8](https://doi.org/10.1088/0004-637X/809/1/8)
- Delrez, L., Gillon, M., Queloz, D., et al. 2018, in *Ground-Based and Airborne Telescopes VII*, Vol. 10700 (SPIE), 446–466, doi: [10.1117/12.2312475](https://doi.org/10.1117/12.2312475)
- Dietrich, J., Apai, D., Schlecker, M., et al. 2023, *EDEN Survey: Small Transiting Planet Detection Limits and Constraints on the Occurrence Rates for Late M Dwarfs within 15 Pc*
- Dorn, C., & Lichtenberg, T. 2021, *The Astrophysical Journal Letters*, 922, L4, doi: [10.3847/2041-8213/ac33af](https://doi.org/10.3847/2041-8213/ac33af)
- Downey, B. G., Nimmo, F., & Matsuyama, I. 2022, *The Thermal-Orbital Evolution of the Earth-Moon System with a Subsurface Magma Ocean and Fossil Figure*
- Dreizler, S., I., J., et al. 2020, *Astronomy & Astrophysics*
- Elkins-Tanton, L. T. 2013, *Nature*, 497, 570, doi: [10.1038/497570a](https://doi.org/10.1038/497570a)

- Emsenhuber, A., Mordasini, C., Burn, R., et al. 2021, *Astronomy & Astrophysics*, 656, A70, doi: [10.1051/0004-6361/202038863](https://doi.org/10.1051/0004-6361/202038863)
- ESA. 2017, PLATO DEFINITION STUDY REPORT (RED BOOK), Tech. Rep. ESA-SCI(2017)1, European Space Agency
- Foreman-Mackey, D. 2016, *Journal of Open Source Software*, 1, 24, doi: [10.21105/joss.00024](https://doi.org/10.21105/joss.00024)
- Fulton, B. J., Petigura, E. A., Howard, A. W., et al. 2017, *The Astronomical Journal*, 154, 109, doi: [10.3847/1538-3881/aa80eb](https://doi.org/10.3847/1538-3881/aa80eb)
- Gaidos, E., Claytor, Z., Dungee, R., Ali, A., & Feiden, G. A. 2023, *Monthly Notices of the Royal Astronomical Society*, stad343, doi: [10.1093/mnras/stad343](https://doi.org/10.1093/mnras/stad343)
- Ginzburg, S., Schlichting, H. E., & Sari, R. 2016, *The Astrophysical Journal*, 825, 29, doi: [10.3847/0004-637x/825/1/29](https://doi.org/10.3847/0004-637x/825/1/29)
- . 2018, *Monthly Notices of the Royal Astronomical Society*, 476, 759, doi: [10.1093/mnras/sty290](https://doi.org/10.1093/mnras/sty290)
- Goldblatt, C. 2015, *Astrobiology*, 15, 362, doi: [10.1089/ast.2014.1268](https://doi.org/10.1089/ast.2014.1268)
- Goldblatt, C., Robinson, T. D., Zahnle, K. J., & Crisp, D. 2013, *Nature Geoscience*, 6, 661, doi: [10.1038/ngeo1892](https://doi.org/10.1038/ngeo1892)
- Goldblatt, C., & Watson, A. J. 2012, *Philosophical Transactions of the Royal Society A: Mathematical, Physical and Engineering Sciences*, 370, 4197, doi: [10.1098/rsta.2012.0004](https://doi.org/10.1098/rsta.2012.0004)
- Gupta, A., & Schlichting, H. E. 2019, *Monthly Notices of the Royal Astronomical Society*, 487, 24, doi: [10.1093/mnras/stz1230](https://doi.org/10.1093/mnras/stz1230)
- Haar, T. H. V., & Suomi, V. E. 1971, *Journal of the Atmospheric Sciences*, 28, 305, doi: [10.1175/1520-0469\(1971\)028<0305:MOTERB>2.0.CO;2](https://doi.org/10.1175/1520-0469(1971)028<0305:MOTERB>2.0.CO;2)
- Hamano, K., Abe, Y., & Genda, H. 2013, *Nature*, 497, 607, doi: [10.1038/nature12163](https://doi.org/10.1038/nature12163)
- Hamano, K., Kawahara, H., Abe, Y., Onishi, M., & Hashimoto, G. L. 2015, *The Astrophysical Journal*, 806, 216, doi: [10.1088/0004-637X/806/2/216](https://doi.org/10.1088/0004-637X/806/2/216)
- Hardegree-Ullman, K. K., Cushing, M. C., Muirhead, P. S., & Christiansen, J. L. 2019, *The Astronomical Journal*, 158, 75, doi: [10.3847/1538-3881/ab21d2](https://doi.org/10.3847/1538-3881/ab21d2)
- Hardegree-Ullman, K. K., Zink, J. K., Christiansen, J. L., et al. 2020, *The Astrophysical Journal Supplement Series*, 247, 28, doi: [10.3847/1538-4365/ab7230](https://doi.org/10.3847/1538-4365/ab7230)
- Harris, C. R., Millman, K. J., van der Walt, S. J., et al. 2020, *Nature*, 585, 357, doi: [10.1038/s41586-020-2649-2](https://doi.org/10.1038/s41586-020-2649-2)
- Irwin, J., Charbonneau, D., Nutzman, P., & Falco, E. 2009, 253, 37, doi: [10.1017/S1743921308026215](https://doi.org/10.1017/S1743921308026215)
- Jin, S., & Mordasini, C. 2018, *The Astrophysical Journal*, 853, 163, doi: [10.3847/1538-4357/aa9f1e](https://doi.org/10.3847/1538-4357/aa9f1e)
- Jin, S., Mordasini, C., Parmentier, V., et al. 2014, *Astrophysical Journal*, 795, doi: [10.1088/0004-637X/795/1/65](https://doi.org/10.1088/0004-637X/795/1/65)
- Kasting, J. F. 1988, *Icarus*, 74, 472, doi: [10.1016/0019-1035\(88\)90116-9](https://doi.org/10.1016/0019-1035(88)90116-9)
- Kasting, J. F., Whitmire, D. P., & Reynolds, R. T. 1993, *Icarus*, 101, 108, doi: [10.1006/icar.1993.1010](https://doi.org/10.1006/icar.1993.1010)
- Kipping, D. M. 2013, *Monthly Notices of the Royal Astronomical Society: Letters*, 434, L51, doi: [10.1093/mnrasl/slt075](https://doi.org/10.1093/mnrasl/slt075)
- Kopparapu, R. K., Ramirez, R., Kasting, J. F., et al. 2013, *The Astrophysical Journal*, 765, 131, doi: [10.1088/0004-637X/765/2/131](https://doi.org/10.1088/0004-637X/765/2/131)
- Leconte, J., Forget, F., Charnay, B., Wordsworth, R., & Pottier, A. 2013, *Nature*, 504, 268, doi: [10.1038/nature12827](https://doi.org/10.1038/nature12827)
- Lichtenberg, T., Schaefer, L. K., Nakajima, M., & Fischer, R. A. 2022, *Geophysical Evolution During Rocky Planet Formation*
- Luger, R., & Barnes, R. 2015, *Astrobiology*, 15, 119, doi: [10.1089/ast.2014.1231](https://doi.org/10.1089/ast.2014.1231)

- Luque, R., & Pallé, E. 2022, *Science*, 377, 1211, doi: [10.1126/science.abl7164](https://doi.org/10.1126/science.abl7164)
- Mazeh, T., Holczer, T., & Faigler, S. 2016, *Astronomy and Astrophysics*, 589, doi: [10.1051/0004-6361/201528065](https://doi.org/10.1051/0004-6361/201528065)
- Montet, B. T., Yee, J. C., & Penny, M. T. 2017, *Publications of the Astronomical Society of the Pacific*, 129, 044401, doi: [10.1088/1538-3873/aa57fb](https://doi.org/10.1088/1538-3873/aa57fb)
- Mordasini, C. 2020, *Astronomy and Astrophysics*, 638, 1, doi: [10.1051/0004-6361/201935541](https://doi.org/10.1051/0004-6361/201935541)
- Mulders, G. D., Ciesla, F. J., Min, M., & Pascucci, I. 2015, *The Astrophysical Journal*, 807, 9, doi: [10.1088/0004-637X/807/1/9](https://doi.org/10.1088/0004-637X/807/1/9)
- Nakajima, S., Hayashi, Y.-Y., & Abe, Y. 1992, *Journal of the Atmospheric Sciences*, 49, 2256, doi: [10.1175/1520-0469\(1992\)049<2256:ASOTGE>2.0.CO;2](https://doi.org/10.1175/1520-0469(1992)049<2256:ASOTGE>2.0.CO;2)
- Nascimbeni, V., Piotto, G., Börner, A., et al. 2022, *Astronomy & Astrophysics*, 658, A31, doi: [10.1051/0004-6361/202142256](https://doi.org/10.1051/0004-6361/202142256)
- Obermeier, C., Koppenhoefer, J., Saglia, R. P., et al. 2016, *Astronomy & Astrophysics*, 587, A49, doi: [10.1051/0004-6361/201527633](https://doi.org/10.1051/0004-6361/201527633)
- Owen, J. E., & Wu, Y. 2013, *Astrophysical Journal*, 775, 1, doi: [10.1088/0004-637X/775/2/105](https://doi.org/10.1088/0004-637X/775/2/105)
- Pierrehumbert, R. T. 2022, *The Runaway Greenhouse on subNeptune Waterworlds*
- Popp, M., Schmidt, H., & Marotzke, J. 2016, *Nature Communications*, 7, 10627, doi: [10.1038/ncomms10627](https://doi.org/10.1038/ncomms10627)
- Puig, L., Pilbratt, G. L., Heske, A., Sanz, I. E., & Crouzet, P.-E. 2016, in *Space Telescopes and Instrumentation 2016: Optical, Infrared, and Millimeter Wave*, Vol. 9904 (SPIE), 649–657, doi: [10.1117/12.2230964](https://doi.org/10.1117/12.2230964)
- Rauer, H. 2021, *PLATO Science Objectives and PLATO Mission Consortium*, doi: [10.5281/zenodo.5585341](https://doi.org/10.5281/zenodo.5585341)
- Rauer, H., Aerts, C., Cabrera, J., & PLATO Team. 2016, *Astronomische Nachrichten*, 337, 961, doi: [10.1002/asna.201612408](https://doi.org/10.1002/asna.201612408)
- Reid, I. N., Turner, E. L., Turnbull, M. C., Mountain, M., & Valenti, J. A. 2007, *The Astrophysical Journal*, 665, 767, doi: [10.1086/519001](https://doi.org/10.1086/519001)
- Rogers, L. A., & Seager, S. 2010, *The Astrophysical Journal*, 712, 974, doi: [10.1088/0004-637X/712/2/974](https://doi.org/10.1088/0004-637X/712/2/974)
- Sato, T., Okuzumi, S., & Ida, S. 2016, *Astronomy & Astrophysics*, 589, A15, doi: [10.1051/0004-6361/201527069](https://doi.org/10.1051/0004-6361/201527069)
- Schlecker, M., Mordasini, C., Emsenhuber, A., et al. 2021, *Astronomy & Astrophysics*, 656, A71, doi: [10.1051/0004-6361/202038554](https://doi.org/10.1051/0004-6361/202038554)
- Sebastian, D., Gillon, M., Ducrot, E., et al. 2021, *Astronomy & Astrophysics*, 645, A100, doi: [10.1051/0004-6361/202038827](https://doi.org/10.1051/0004-6361/202038827)
- Skilling, J. 2004, *AIP Conference Proceedings*, 735, 395, doi: [10.1063/1.1835238](https://doi.org/10.1063/1.1835238)
- Speagle, J. S. 2020, *Monthly Notices of the Royal Astronomical Society*, doi: [10.1093/mnras/staa278](https://doi.org/10.1093/mnras/staa278)
- Spergel, D., Gehrels, N., Baltay, C., et al. 2015, *Wide-Field Infrared Survey Telescope-Astrophysics Focused Telescope Assets WFIRST-AFTA 2015 Report*, doi: [10.48550/arXiv.1503.03757](https://doi.org/10.48550/arXiv.1503.03757)
- Szabó, G. M., & Kiss, L. L. 2011, *Astrophysical Journal Letters*, 727, 2, doi: [10.1088/2041-8205/727/2/L44](https://doi.org/10.1088/2041-8205/727/2/L44)
- Thompson, S. E., Coughlin, J. L., Hoffman, K., et al. 2018, *The Astrophysical Journal Supplement Series*, 235, 38, doi: [10.3847/1538-4365/aab4f9](https://doi.org/10.3847/1538-4365/aab4f9)
- Turbet, M., Bolmont, E., Ehrenreich, D., et al. 2020, *Astronomy & Astrophysics*, Volume 638, id.A41, <NUMPAGES>10</NUMPAGES> pp., 638, A41, doi: [10.1051/0004-6361/201937151](https://doi.org/10.1051/0004-6361/201937151)

- Turbet, M., Ehrenreich, D., Lovis, C., Bolmont, E., & Fauchez, T. 2019, *Astronomy & Astrophysics*, 628, A12, doi: [10.1051/0004-6361/201935585](https://doi.org/10.1051/0004-6361/201935585)
- Unterborn, C. T., Hinkel, N. R., & Desch, S. J. 2018, *Research Notes of the AAS*, 2, 116, doi: [10.3847/2515-5172/aacf43](https://doi.org/10.3847/2515-5172/aacf43)
- Van Eylen, V., Agentoft, C., Lundkvist, M. S., et al. 2018, *Monthly Notices of the Royal Astronomical Society*, 479, 4786, doi: [10.1093/mnras/sty1783](https://doi.org/10.1093/mnras/sty1783)
- Virtanen, P., Gommers, R., Oliphant, T. E., et al. 2020, *Nature Methods*, 17, 261, doi: [10.1038/s41592-019-0686-2](https://doi.org/10.1038/s41592-019-0686-2)
- Watson, A. J., Donahue, T. M., & Walker, J. C. G. 1981, *Icarus*, 48, 150, doi: [10.1016/0019-1035\(81\)90101-9](https://doi.org/10.1016/0019-1035(81)90101-9)
- Youdin, A. N. 2011, *Astrophysical Journal*, 742, doi: [10.1088/0004-637X/742/1/38](https://doi.org/10.1088/0004-637X/742/1/38)
- Zeng, L., Sasselov, D. D., & Jacobsen, S. B. 2016, *The Astrophysical Journal*, 819, 127, doi: [10.3847/0004-637X/819/2/127](https://doi.org/10.3847/0004-637X/819/2/127)